Enhancing the Perturbation Injection Capabilities of Grid-Connected Converters With Asymmetric Signals

Jules MACE, Andrea CERVONE, and Drazen DUJIC

Abstract—**Impedance identification is an important tool for the evaluation of grid-converter interactions, and it is based on the injection of a controlled small signal perturbation and in the analysis of the corresponding system response. Using already installed grid-connected converters as perturbation sources offers the advantage of avoiding additional dedicated hardware, but faces some implementation challenges caused by the limited voltage reserve that is normally available in such equipment. To overcome this limitation, this work presents perturbation injection signals that, by considering asymmetric voltage limits, can make the best use of the limited voltage reserve available in the system. The developed approach is first presented for a periodic multi-tone perturbation injection, and then it is extended for narrow-band and wide-band perturbations. Analytical, numerical and experimental results prove that the proposed solution can provide perturbation injections with considerably higher magnitudes compared to other conventional approaches, which makes it ideal to enhance the perturbation injection capabilities of existing grid-connected converters.**

Index Terms—**Impedance identification, grid connected converters, perturbation injection.**

I. Introduction

THE recent years have witnessed a progressive growth of grid-connected converters in many application areas, ranging from distributed energy resources, HVDC transmission, battery energy storage systems and electric vehicles charging stations. This proliferation of converter-based systems has brought concerns about grid stability among electric grid operators, especially since some instability accidents have occurred [1]–[3]. The reason for such instability events has been attributed to the incompatibility between the equivalent impedance of the grid and the equivalent admittance of the converters that, once connected to one another, can interact and lead to increasingly amplifying oscillations, with potentially catastrophic outcomes.

As a result, impedance identification has become a relevant research area in the field of power electronics. The realtime estimation of the equivalent impedance of the grid or of a grid-connected equipment allows monitoring the correct operation of a network [4]–[6], detecting grid reconfigurations [7], [8], and potentially adapting grid-connected converters during operation [9], [10].

The impedance estimation is based on the injection of controlled small-signal perturbations in the system, and on the analysis of the corresponding small-signal response. The perturbations should be small to avoid altering the steadystate operation of the system, while also possess adequate magnitude to be detectable by the sensing equipment [11].

These perturbations can be generated by ad-hoc perturbation injection converters (PICs) [12], [13], allowing precise shaping of the perturbation injected, of the desired injection time, magnitude and frequency content. However, installing dedicated hardware for perturbation injection purposes might be inconvenient or impractical, especially when cost or space constraints within the network are taken into account [14], [15].

Therefore, it would be convenient to use the same existing grid-connected converters as perturbation injection sources [3], [16]. In this case, by superimposing a small-signal perturbation on top of the steady-state operating waveforms of an existing converter, the impedance identification could be achieved without any additional hardware. Nevertheless, as of today, the majority of grid-connected converters are not inherently designed for perturbation injection purposes, which results in inherent limitations and challenges.

One of these challenges comes from the restricted bandwidth of grid-connected converters. This aspect, which has been thoughtfully addressed in [17], imposes an upper limit on the bandwidth of the injected perturbation signals, which is primarily determined by the switching frequency of the semiconductor devices and by the sampling frequency of the adopted controller platforms. Nevertheless, considering the ongoing advancements in the semiconductor devices technology (and particularly in wide-bandgap devices) and the increasing availability of faster control platforms (including DSP and FPGA boards), this limitation is expected to become progressively less restrictive in the upcoming years.

Another major challenge in using existing grid-connected converters for perturbation injection purposes comes from a limited voltage reserve, which refers to the difference between the maximum voltage that the converter is capable of applying and the voltage of its specific operating condition. Indeed, most existing grid-connected converters are designed to operate with a limited DC-bus voltage and at high modulation indexes

---

Manuscript received June 18, 2024; revised July 11, 2024; accepted August 2, 2024. Date of publication September 30, 2024; date of current version August 30, 2024. This work was supported by the Horizon 2020 Framework Programme (EU) under Grants 957788. *(Corresponding author: Jules Mace.)*

All authors are with the Power Electronics Laboratory (PEL) of the École Polytechnique Fédérale de Lausanne (EPFL), Lausanne, Switzerland (e-mail: jules.mace@epfl.ch; andrea.cervone@epfl.ch; drazen.dujic@epfl.ch).

Digital Object Identifier 10.24295/CPSSTPEA.2024.00017

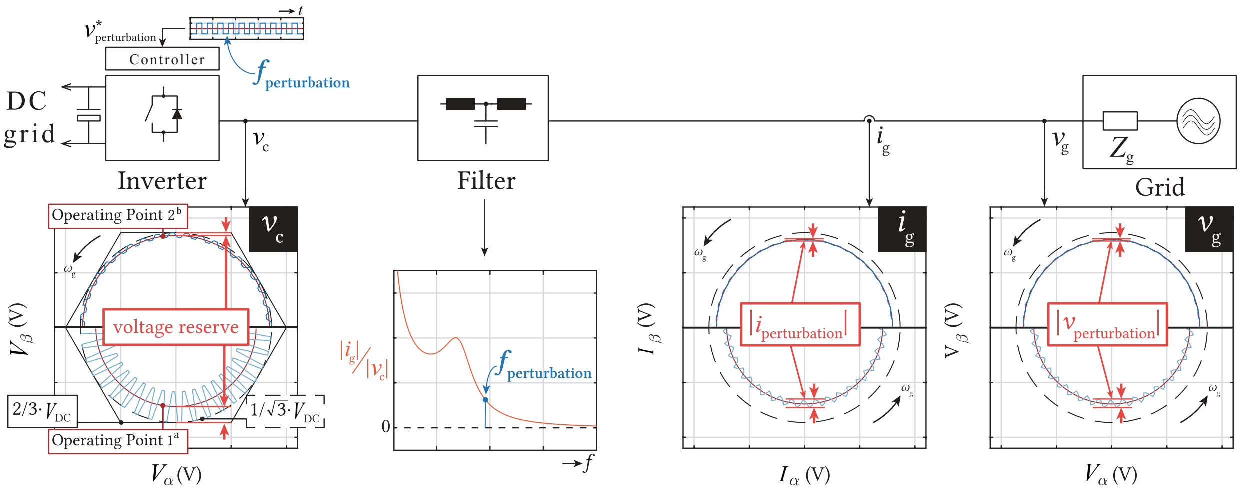

Fig. 1. Effect of a different voltage reserves on the perturbation injection capabilities of a grid-connected converter.
a: On the bottom graphs (Operating Point 1), a sufficiently high voltage reserve allows the converter to inject a perturbation of high magnitude that, even after the filtering elements, can still be measured reliably.
b: On the top graphs (Operating Point 2), the fundamental converter voltage is close to the available voltage limit. Then, the voltage reserve is severely reduced, and the resulting perturbations after the filtering element may be hard to detect from the adopted sensing equipment.

in rated conditions. This leads to a small voltage reserve available for perturbation injection purposes, which could be even worsened considering that, according to grid codes, the AC voltage magnitude can be subject to a 10% variation in ordinary operation.

Furthermore, the perturbation injection capabilities of the converter are even worsened by the presence of the AC filtering elements (i.e., L, LCL, etc.). Indeed, in order to mitigate the effect of the pulse-width modulation (PWM) harmonics, these filters show a low-pass behavior and introduce an increasingly stronger attenuation above the fundamental frequency. This means that, depending on the grid impedance and on the parameters of the AC filter, a voltage perturbation measured at the point of common coupling with the grid could be just a small percentage of the voltage perturbation generated at the output terminals of the converter.

Finally, the signals to be measured for the impedance identification are generally of small magnitude, and superimposed on top of the large fundamental signals of voltage and current at 50 Hz or 60 Hz, which make their measurement more challenging and subject to uncertainty, thus compromising the reliability of the impedance identification itself.

As a result, if one wants to employ an existing grid-connected converter as a perturbation injection source, it is crucial to understand how the injected perturbations can be maximized coherently with the available parameters. This aspect is analyzed in this work, which focuses on identifying what is the most effective perturbation signal that can be adopted to optimally use the limited available voltage reserve.

In what follows, it is shown that most of the conventional signals that are used for perturbation injection purposes, in both single-tone [18] or multi-tone injections [3] and in widebandwidth injections [17], [19], do not utilize the available voltage reserve effectively, weakening the perturbation injection capability of a grid-connected converter. On the contrary, a limited voltage reserve can be better utilized by exploiting asymmetric perturbation signals, tailor designed to take into account the asymmetric constraints of the system. So far, the specific advantages of asymmetric perturbation injections for impedance identification have not been explored in the technical literature, and the question of which type of signal provides the most advantages remains unanswered. In this framework, this work derives an optimal asymmetric signal aimed at maximizing the perturbation injection with the limited available voltage reserve.

The rest of this paper is organized as follows: first, Section II discusses the effect of a limited voltage reserve on the perturbation injection capabilities of a grid-connected converter. Then, Section III explains how asymmetric signals can be utilized to better exploit the converter capabilities. An optimal asymmetric signal is found to maximize the fundamental magnitude of the injected perturbation, and an extension to narrow-band and wide-band perturbations is presented. After that, Section IV shows the experimental validation of the proposed signal, proving its benefits over conventionally adopted symmetric perturbations. Finally, Section V summarizes the conclusions of this work.

II. Effect of a Limited Voltage Reserve on the Perturbation Injection Capabilities

Consider a voltage source converter connected to the three-phase AC grid, as schematically represented in Fig. 1.

The AC grid can be modeled in the Laplace domain as an equivalent Thevenin source, consisting of an ideal sinusoidal voltage source v_{grid} and an equivalent series-connected impedance Z_g. The terminal voltage that is available at the point of common coupling can be expressed as:

$$v_g = v_{\text{grid}} + Z_g \bullet i_g \tag{1}$$

The estimation of Z_g requires generating a small-signal perturbation on v_g and analyzing the corresponding small-signal response on i_g. As previously mentioned, these perturbations should be small enough not to alter the steady-state operation of the system, but at the same time they should be high enough to be detectable by the adopted sensing equipment. Normally, they are injected in the synchronous reference frame, in a way to estimate the *dq* impedances matrix of the system.

The grid-connected converter itself could be used as a perturbation injection source, which can be achieved by superimposing a perturbation on top of the fundamental AC voltage $v_{c,AC}$ generated at its terminals. However, because of the presence of a filter located between the converter terminals and the point of common coupling, the perturbation obtained on v_g is not equal to the one applied on v_c. This is especially relevant for relatively high-frequency perturbations, since filters conventionally adopted in grid-connected converters (e.g., L, LC, LCL, etc.) exhibit a low-pass characteristic that introduces a considerable attenuation above the fundamental AC frequency. This effect poses some challenges for the impedance identification, as the magnitude of the perturbations measured on v_g and i_g may be so small to be comparable to the noise or to the uncertainty levels of the transducers, potentially leading to unreliable results.

This effect could be mitigated by increasing the magnitude of the perturbation applied on v_c. However, since this perturbation is injected on top of the fundamental waveform of the converter, its magnitude is intrinsically constrained by the operating conditions of the system. This constraint can be represented by introducing the concept of the voltage reserve, here defined as the difference between the maximum voltage that could be applied by the converter and the fundamental AC voltage generated under specific operating conditions:

$$v_{res} = |v_{c,MAX}| - |v_{c,AC}| \tag{2}$$

The maximum voltage $|v_{c,MAX}|$ depends of the DC-link voltage V_{DC} of the converter and, as known, it is limited to $|v_{c,MAX}| = V_{DC}/\sqrt{3}$ for a three-wire system when a zero sequence injection is applied to the modulator, while it is limited to $|v_{c,MAX}| = V_{DC}/2$ in presence of a neutral wire (in which case the zero-sequence injection cannot be applied).

The fundamental converter voltage $v_{c,AC}$, on the other hand, depends on many parameters, including the converter output filter, the grid impedance, the fundamental AC grid voltage and the active/reactive power flows. As a result, given the system parameters, the generated converter voltage $v_{c,AC}$ can change in real-time depending on the specific operating conditions, which can influence the available voltage reserve v_{res} and, consequently, the perturbation injection capabilities of the converter. This aspect is graphically illustrated in Fig. 1.

The Operating Point 1, shown in the bottom graphs of Fig. 1, refers to the condition with a relatively high voltage reserve, that allows injecting high magnitude perturbations on v_c. In this case, even considering the attenuation introduced by the filtering elements, the magnitude of the resulting perturbations on v_g and i_g would be still be high enough to guarantee a reliable estimation of the grid impedance Z_g.

On the contrary, the Operating Point 2, shown in the top graphs of Fig. 1, refers to the condition with a relatively small voltage reserve, that limits the magnitude of the perturbation that can be injected on v_c. In this case, after the attenuation introduced by the filter, the magnitude of the resulting perturbation on v_g and i_g could be so small to be practically indistinguishable from the sensor noise, and the grid impedance estimation would not provide reliable results.

Since existing grid connected converters are normally designed to work with a limited DC-link voltage and to operate at high modulation index, the limited voltage reserve poses considerable challenges for perturbation injection purposes. Considering, for example, a standard 400 V–50 Hz three-phase AC grid, most of the commercially available grid-connected converters are designed with a DC-bus voltage in the range 700–750 V, typically employing 2 × 400 V or 2 × 450 V capacitors and 1200 V rated semiconductor devices. Assuming a voltage drop on the filtering elements of around 30 V peak (e.g., considering, for example, a 1 mH filter for a 50 kVA rated converter), the nominal operation requires a modulation index of around $M_{ind} \approx 0.9$–1.0, leaving a voltage reserve of around 50–80 V. Assuming a 20 dB attenuation at the perturbation frequency $f_p \gg 50$ Hz due to the filtering elements, this leads to a voltage perturbation of around 5–8 V (i.e., 1.5%–2.5% of the fundamental). This limited voltage injection capability is even worsened in case of a 10% increase of the fundamental AC voltage of the grid, in which case the converter modulation index would be in the range $M_{ind} \approx 1.0$–1.1, and the voltage reserve would be around 10–35 V which, considering the same filtering parameters, would result in a perturbation of just 1–3.5 V (i.e., 0.3%–1.1% of the fundamental).

In light of these aspects, it is of practical interest to investigate the maximum theoretical limits of perturbation injection capabilities within voltage reserve constraints, as analyzed in what follows.

III. ENHANCING THE PERTURBATION INJECTIONS USING ASYMMETRIC SIGNALS

Most signals that are conventionally used for parameter identification purposes are symmetric, featuring equal positive and negative peak values centered around zero. These include both signals adopted to inject perturbations at specific frequencies, like single-tone and multi-tone signals [3], and signals used to apply narrow-band or wide-band perturbations, like chirps [19] or pseudo-random binary sequences (PRBS) [6].

If a symmetric signal is superimposed to the fundamental AC voltage generated by a grid-connected converter, the peak value of the resulting waveform is limited to the maximum voltage $|v_{c,MAX}|$ that the converter is capable of generating based on its DC-link voltage. However, symmetric perturbation signals do not make the best utilization of the available voltage reserve. Indeed, using asymmetric perturbation signals, with positive and negative peaks not centered around zero, could allow increasing the magnitude of the injected perturbation

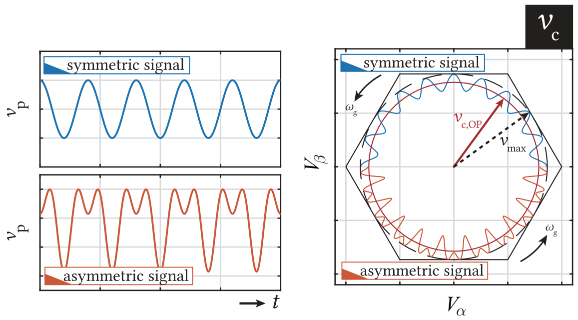

Fig. 2. Example of a symmetric and an asymmetric perturbation signal. The asymmetric signal has a much larger perturbation amplitude compared to the symmetric signal.

harmonics without violating the peak voltage constraints. An example of how an asymmetric signal can better utilize a limited voltage reserve is graphically represented in Fig. 2.

Many different asymmetric signals could be generated to inject controlled perturbations. Similarly to conventional symmetric signals, also asymmetric ones can be designed to perturb the system only at specific frequencies (i.e., generating a multi-tone spectrum) or to provide a continuous spectrum sweeping a frequency band of interest. In what follows, a specific asymmetric perturbation signal is discussed, that can be of special interest for perturbation injection purposes.

A. Optimal Asymmetric Injection Signal

Consider the case for which a grid-connected converter is required to perturb the system at a specific frequency f_p. It could be of interest to find the perturbation signal that would allow the best utilization of the available voltage reserve. In this framework, it is possible to define a maximum threshold K^+ and a minimum threshold K^- and search for an optimal perturbation signal $v_p(t)$ such that:

- the maximum value of $v_p(t)$ is limited to K^+, in a way not to overcome the maximum voltage that can be generated by the converter;
- the minimum value of $v_p(t)$ is limited to K^-, in a way not to overcome the minimum voltage that can be generated by the converter;
- the average value of $v_p(t)$ in the period $T_p = 1/f_p$ is zero, in a way that the perturbation does not affect the steady-state operating point of the system in order to minimize the impact of the perturbation on the converter operation and grid control;
- the magnitude of the first harmonic of $v_p(t)$ in the period $T_p = 1/f_p$ is maximized, in a way to provide the highest possible perturbation under the system constraints.

These requirements can be formulated mathematically as the constrained optimization problem:

$$\max_{v_p(t)}\left\{\left|v_p(f_p)\right|\right\} \text{subject to} \begin{cases} K^- \leqslant v_p(t) \leqslant K^+ \\ \left|v_p(0)\right| = 0 \end{cases} \tag{3}$$

with the average value $|v_p(0)|$ of $v_p(t)$ and the fundamental magnitude $|v_p(f_p)|$ of $v_p(t)$ respectively given by:

$$\left|v_p(0)\right| = \frac{1}{T_p}\int_0^{T_p} v_p(t)\,\mathrm{d}t \tag{4}$$

$$\left|v_p(f_p)\right| = \frac{2}{T_p}\left|\int_0^{T_p} v_p(t)\,e^{-j2\pi f_p t}\,\mathrm{d}t\right| \tag{5}$$

The problem (3) is the optimization of a functional depending on the function $v_p(t)$. It can be proven (see Appendix) that the optimal solution is the asymmetric rectangular signal:

$$v_{p,\,opt}(t) = \begin{cases} K^+, & \text{for } 0 \leqslant t < \delta T_p \\ -K^-, & \text{for } \delta T_p \leqslant t < T_p \end{cases} \tag{6}$$

where δ is the equivalent duty-ratio of the rectangular signal, and is equal to:

$$\delta = \frac{T_{K^+}}{T_{K^+} + T_{K^-}} = \frac{K^-}{K^+ + K^-} \tag{7}$$

The signal $v_{p,opt}(t)$ has a zero average value over T_p, and only assumes the values K^+ and $-K^-$. As also previously mentioned, since $v_{p,opt}(t)$ has a zero average value (as imposed in (3)), if it is applied as a perturbation in the synchronous reference frame, it would not interfere with the steady-state operation of the converter.

Fig. 3 shows a graphical representation of $v_{p,opt}(t)$ for different (K^-/K^+) ratios, while Fig. 4 shows the corresponding harmonic spectra. As can be seen, only in case $K^+ = K^-$ (equal positive and negative limits), $v_{p,opt}(t)$ degenerates into a symmetrical square-wave with 50% duty-ratio.

From (6), it is possible to analytically compute the magnitude of the fundamental component of $v_{p,opt}(t)$, which is:

$$\left|v_{p,\,opt}(f_p)\right| = \frac{4}{\pi}\,\frac{K^+ + K^-}{2}\,\sin\left(\pi\frac{K^-}{K^+ + K^-}\right) \tag{8}$$

A graphical representation of the fundamental magnitude $v_{p,opt}(f_p)$ for varying (K^-/K^+) ratios is shown in Fig. 5. As can be seen, the fundamental magnitude of the perturbation starts from the value of $(4/\pi)\,K^+$ when $(K^-/K^+) = 1$ (i.e., when $v_{p,opt}(t)$ is equivalent to a symmetric square-wave signal), and it progressively increases with the (K^-/K^+) ratio, approaching the limit of $2K^+$.

As a result, the proposed optimal signal allows up to 100% increase compared to a sinusoidal single-tone perturbation signal (for which $|v_{p,sin}(f_p)| = K^+$) and up to a 55% increase compared to a symmetrical square-wave perturbation signal (for which $|v_{p,sqr}(f_p)| = (4/\pi)\,K^+$).

However, it can also be noted that the increase of $|v_{p,opt}(f_p)|$ is progressively less relevant as the ratio (K^-/K^+) increases and, beyond a ratio of around 6–8, a further increase of K^- does not provide significant benefits.

Finally, a further analysis of the spectrum of $v_{p,opt}$ in Fig. 4 also shows the appearance of additional higher-order harmonics compared to a symmetric square-wave signal. Although not necessary for impedance identification at the frequency f_p, these higher order harmonics can be used as supplementary perturbation harmonics for impedance identification at higher

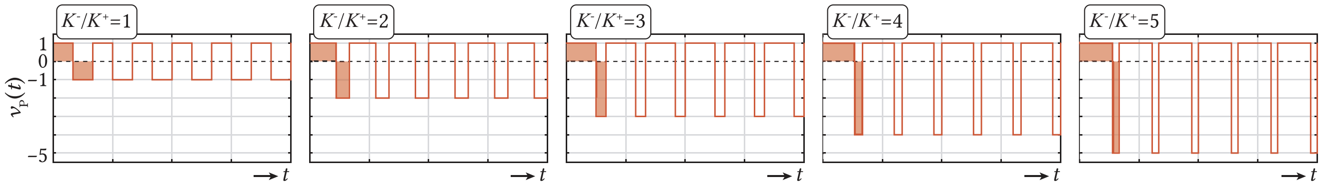

Fig. 3. Time waveform of the optimal asymmetric signal for varying (K^-/K^+) ratio (considering a fixed maximum value $K^+ = 1$).

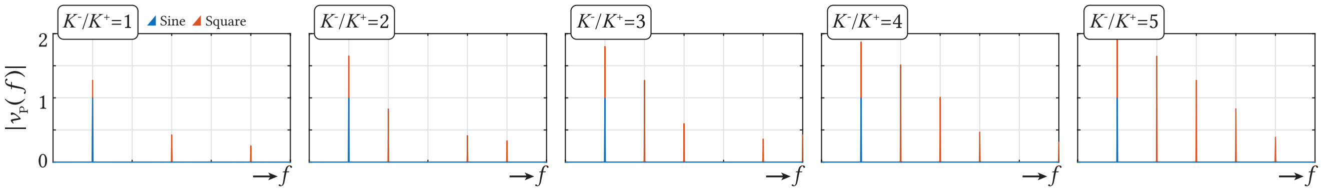

Fig. 4. Harmonic spectrum of the optimal asymmetric signal for varying (K^-/K^+) ratio (considering a fixed maximum value $K^+ = 1$).

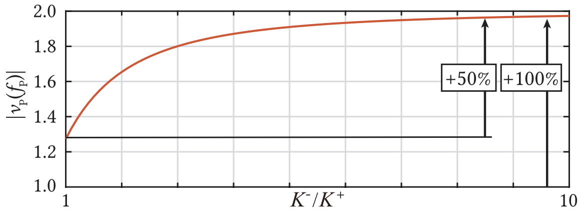

Fig. 5. Magnitude of the fundamental component $|v_{p,\text{opt}}(f_p)|$ of the proposed asymmetrical rectangular signal for different (K^-/K^+) ratios (considering $K^+ = 1$).

frequencies. The ratio (K^-/K^+) not only impacts the harmonic shape but also the harmonic magnitude and as the ratio increases, the harmonic magnitudes tend to increase along with it.

B. Extension to Asymmetric Chirp Signals

The optimal asymmetric signal introduced in the previous section has been defined based on a specific fundamental frequency f_p for the desired perturbation injection, and results in a multi-tone spectrum whose spectrum is concentrated at fundamental frequency harmonics. However, also asymmetric signals can be adapted in a way that all the frequencies in a specific range of interest are excited at once, similarly to how it is conventionally done for conventional chirp perturbations.

A simple way to perform this extension is by replacing the fixed frequency f_p with a frequency sweep that covers a desired range [$f_{\text{chirp,beg}}$, $f_{\text{chirp,end}}$]. In practical implementations, this can be done using the scheme represented in Fig. 6, which shows how a conventional chirp generator can be adapted by replacing the sinusoidal waveform with the optimal asymmetric signal defined in (6).

To exemplify this concept, Fig. 7 provides a comparison between a conventional sine chirp, a symmetrical square-wave chirp and an asymmetrical rectangular chirp. The symmetrical square chirp signal has been proposed and characterized in [20] and then utilized for impedance estimation in [21], [22], using a dedicated perturbation injection device. In Fig. 7, the signals are analyzed using the same maximum value K^+ and the same linearly increasing frequency sweep:

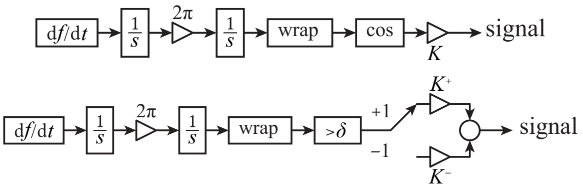

Fig. 6. Block diagram for the generation of perturbation signals with variable frequency. Top) Based on a conventional sine-wave generator. Bottom) Based on the asymmetrical rectangular signal defined in (6).

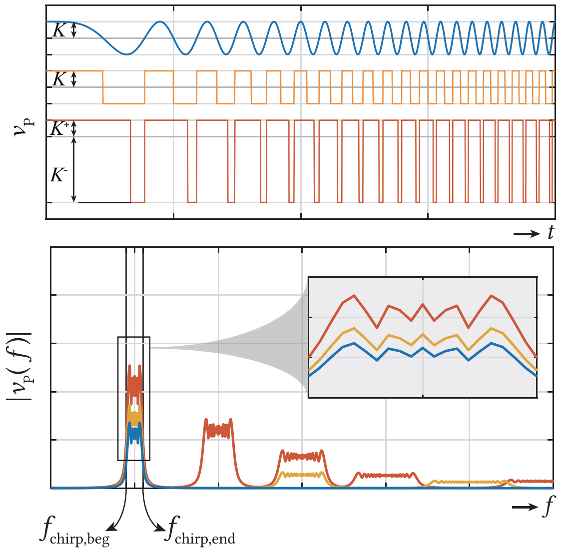

Fig. 7. Example of generation of different signal chirps using a linearly increasing frequency sweep. Top) Time domain. Bottom) Frequency domain.

$$f_{\text{chirp}}(t) = f_{\text{chirp, beg}} + (f_{\text{chirp, end}} - f_{\text{chirp, beg}})\cdot\frac{t}{T_{\text{chirp}}} \tag{9}$$

To facilitate the visualization, the harmonic spectra in Fig. 7 have been drawn including an envelope connecting various frequency beams.

As can be noted, the spectrum of the three signals exhibit analogous characteristics to the ones previously observed for

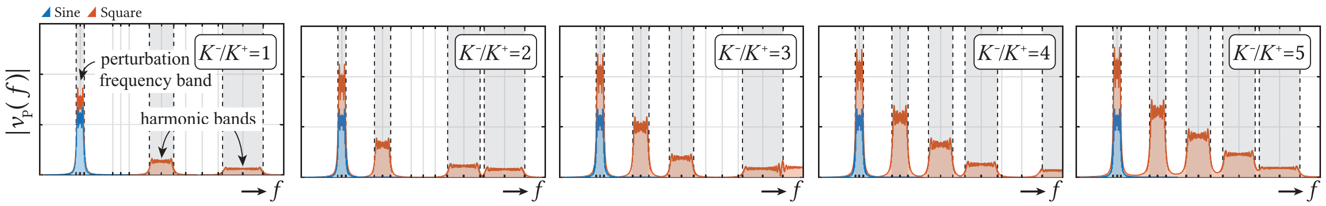

Fig. 8. Harmonic spectrum of the proposed asymmetric signal used with a frequency sweep for varying (K^-/K^+) ratio.

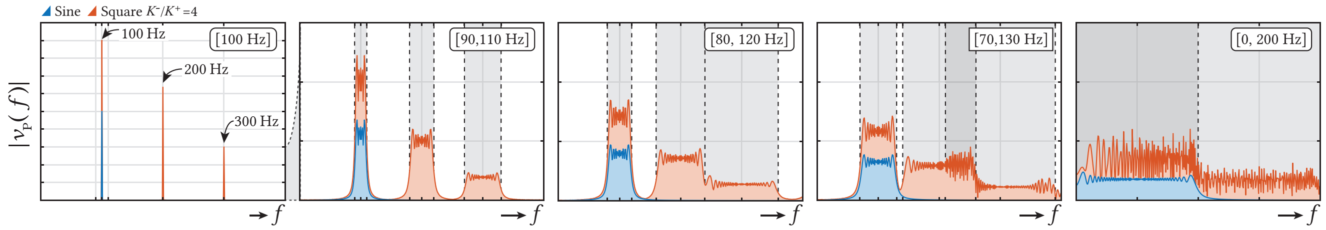

Fig. 9. Harmonic spectrum of the proposed asymmetric signal used with a frequency sweep for varying [$f_{\text{chirp,beg}}$,$f_{\text{chirp,end}}$] range.

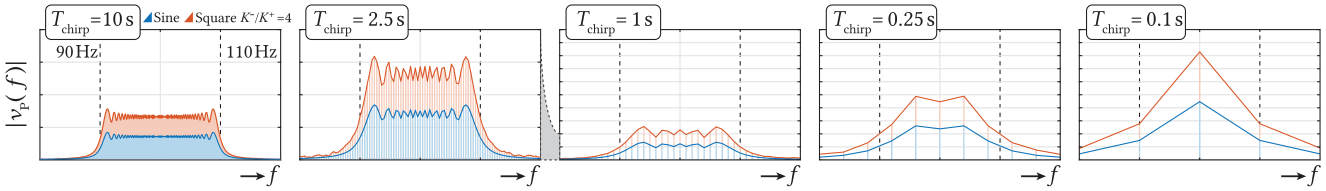

Fig. 10. Harmonic spectrum of the proposed asymmetric signal used with a frequency sweep for varying rising time T_{chirp}.

a fixed generation frequency. In this case, the spectrum of the sine chirp is predominantly concentrated in the frequency range [$f_{\text{chirp,beg}}$, $f_{\text{chirp,end}}$], and it has negligible effect elsewhere. Conversely, the spectrum of the symmetrical squarewave chirp not only shows a higher magnitude in the same frequency band of interest, but it also introduces additional harmonic bands at the odd multiples of the central frequency $f_{\text{chirp,center}} = (f_{\text{chirp,beg}} + f_{\text{chirp,end}})/2$. Finally, the asymmetrical rectangular chirp shows an even higher magnitude in the desired frequency band, and additional higher-order harmonic bands are also present at the even and odd multiple integers of the central generation frequency. As a result, also in this case the asymmetrical signal derived in (6) provides a higher magnitude compared to conventional symmetrical signals, which can be beneficial for impedance estimation purposes. The higher order harmonic bands of the asymmetric square chirp signal, despite not being indispensable for impedance identification (since the frequency sweep [$f_{\text{chirp,beg}}$, $f_{\text{chirp,end}}$] of the chirp can be anyhow selected by design), can still be used to get extra information about the system impedance at higher frequencies, without need to modify the a-priori defined perturbation injection signal (and, hence, without requiring additional measurement recordings).

Figs. 8−10 show the harmonic spectrum of the proposed asymmetric chirp signal for different (K^-/K^+) ratios, for different frequency bands [$f_{\text{chirp,beg}}$, $f_{\text{chirp,end}}$] and for different rise times T_{chirp}, respectively. For comparison, a conventional sine chirp is also shown in the figures, using the same magnitude K^+ and the same frequency sweep $f_{\text{chirp}}(t)$.

As can be seen from Fig. 8, the change in the (K^-/K^+) ratio follows a similar pattern as in Fig. 4. The magnitude of the harmonics in the range [$f_{\text{chirp,beg}}$, $f_{\text{chirp,end}}$] increases with K^- following the same trend as in (8), which was graphically represented in the diagram of Fig. 5. At the same time, additional higher order harmonic bands appear around the multiple integers of the center frequency. Compared to the fundamental band, the higher-order harmonic bands are characterized by a smaller magnitude, but are more spread in the frequency domain.

The effect of the frequency spread is even more evident in Fig. 9. It can be noted that as the frequency band [$f_{\text{chirp,beg}}$, $f_{\text{chirp,end}}$] expands, the width of all harmonic bands also increases, while their average magnitude gradually diminishes. This shows how the energy of the signal is distributed across a progressively broader frequency range.

As the frequency sweep is enlarged, it also becomes evident that various harmonic bands begin to merge and interact with each other. This phenomenon introduces an aliasing effect, resulting in a less uniform magnitude spectrum of the signal, which is particularly pronounced in the last two graphs of Fig. 9. Here, some harmonic components experience an amplification due to aliasing, while others undergo a reduction in magnitude. Nevertheless, on average within the desired frequency range [$f_{\text{chirp,beg}}$, $f_{\text{chirp,end}}$] used for the sweep, the magnitude spectrum achieved through the proposed signal remains consistently higher than the one obtained with a conventional sine chirp.

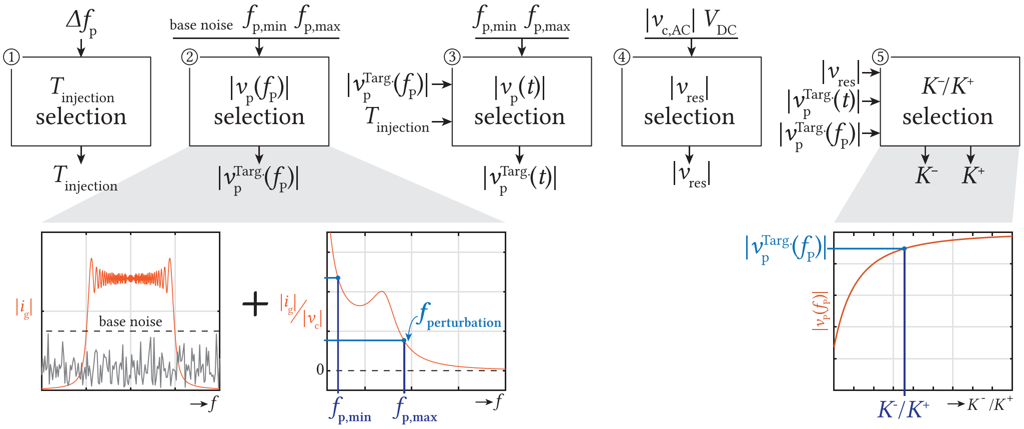

Fig. 11. $T_{injection}$, K^+ and K^- selection procedure.

Finally, Fig. 10 shows the effect of varying the rising time T_{chirp} of the frequency sweep. In general, longer rising times result in a more evenly spread spectrum within the desired frequency range $[f_{chirp,beg}, f_{chirp,end}]$, and multiple harmonic components are excited simultaneously. In contrast, reducing T_{chirp} decreases the number of frequency components in the signal (as evident from the increased spacing between different harmonic beams in the spectra of Fig. 10). At the same time the magnitude of the excited harmonics is progressively increased, indicating that the energy of the signal becomes progressively concentrated on a reduced number of harmonics.

C. Injection Parameters Selection

For an asymmetric signal to be employed for perturbation injection in a grid, two main parameters need to be selected: the injection time $T_{injection}$ and the K^-/K^+ ratio. To do so, two main objectives need to be satisfied. Firstly, the perturbation signal must cover all the frequencies of interest and secondly, it must have magnitudes larger than the base noise level in order to be measurable and meaningful. Based on those constraints, a step-by-step parameter selection procedure can be followed:

1) $T_{injection}$ selection: The injection time defines the gap Δf_p between two perturbation frequency points $f_{p,k}$ and $f_{p,k+1}$:

$$\Delta f_p = f_{p,k+1} - f_{p,k} = \frac{1}{T_{injection}} \tag{10}$$

A longer injection time will hence lead to a lower gap and therefore, more frequency points in the perturbation spectrum.

2) Perturbation magnitude $|v_p^{TARGET}(f_p)|$ selection: The perturbation magnitude has to be selected so that the converter output current $|i_c(f_p)|$ is significantly larger than the base noise. This can be selected based on the converter filter characteristics.

3) Perturbation amplitude $|v_p^{TARGET}(t)|$ selection: Based on the targeted perturbation magnitude $|v_p(f_p)^{TARGET}|$ and on the injection time, the perturbation amplitude $|v_p(t)|$ can be found. For a sinesweep ranging from $f_{p,min}$ to $f_{p,max}$ with a constant amplitude $|v_p(t)|$, the perturbation magnitude for each perturbation frequency point is on average:

$$|v_p(f_p)| = |v_p(t)| \cdot \frac{1}{\sqrt{N_p}} \tag{11}$$

with $N_p = T_{injection} \cdot (f_{p,max} - f_{p,min})$.

Therefore, the perturbation magnitude can be found as:

$$|v_p^{TARGET}(t)| = |v_p^{TARGET}(f_p)| \cdot \sqrt{T_{injection} \cdot (f_{p,max} - f_{p,min})} \tag{12}$$

4) Perturbation amplitude $|v_p^{TARGET}(t)|$ selection: By tracking the converter voltage magnitude $|v_{c,AC}|$, the voltage reserve can be computed.

5) K^-/K^+ ratio computation: the ratio can be selected based on two situations: If the voltage reserve is larger than the desired voltage perturbation amplitude $|v_p^{TARGET}(t)|$, a sinesweep canbe used. On the other hand, if the voltage reserve is lower than the desired voltage perturbation magnitude, an asymmetric perturbation can be employed in order to increase the desired perturbation magnitude $|v_p^{TARGET}(f_p)|$. The perturbation amplitude K^+ will be defined by the voltage reserve and the ratio can be found based on the curve from Fig. 5.

The procedure is summarized in Fig. 11.

Finally, it is worth pointing out that the analyzed perturbation injection signal is introduced in the converter reference voltages (i.e., before the PWM algorithm). Therefore, the finite resolution of the switching and control frequency of the converter poses a limitation in the quality of the perturbation signal that can be generated at its output terminals. Indeed, the sharp commutation edges of the square signal might be slightly shifted if the transitions are not synchronized with the switching instants of the PWM.

However, as long as the base injection frequency of the perturbation signal is enough lower than the control/switching frequency of the converter, the effect of this limited resolution are negligible. Indeed, the effects of the time resolution mainly affects the higher order harmonic bands of the signal spectrum, while the base band is only influenced in a minor way by aliasing effects. Furthermore, considering that the impedance identification is anyhow obtained by post-processing the

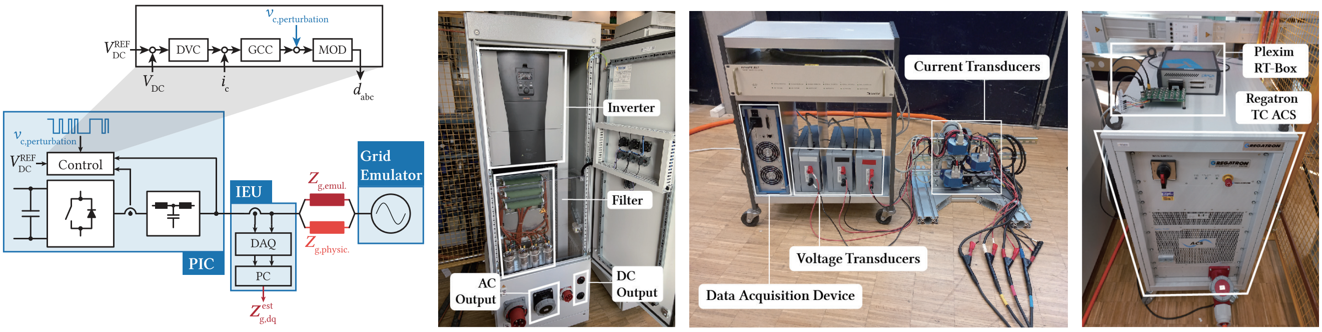

(a) (b) (c) (d)

Fig. 12. Impedance measurement setup. (a) Circuit diagram. (b) Active-front-end (AFE), with integrated perturbation injection capabilities. (c) Impedance estimation unit (IEU). (d) Grid Emulator.

simultaneous voltage and current samples, even a slightly distorted perturbation signal can generate at the converter output some measurable quantities (above the noise level threshold), that can be exploited for a reliable impedance identification.

IV. Experimental Validation

A. Experimental Setup

The advantages of the proposed perturbation injection approach over conventional solutions have been validated experimentally using the setup represented in Fig. 12.

A commercially available 45 kVA-rated active front end (AFE) converter, based on a Hyundai N700 hardware, has been used as the main investigation platform. To allow for software reconfiguration, the control platform of the AFE has been replaced by a Texas Instruments TMS320F28335 DSP, which has been interfaced to the power hardware through a LARA 100 GCC Box developed by PERUN Technologies. A Schaffner FN6840 LCL filter has been used for the interconnection to the AC grid.

The AFE has been controlled using a standard grid-following approach, with the aim of stabilizing the DC bus voltage to a constant reference value and, at the same time, absorbing or injecting a controlled reactive power to the AC grid. Its control software has been extended with perturbation injection features, allowing to superimpose any desired voltage perturbation on top of its fundamental *dq* voltage references.

The AFE and the filter are shown in Fig. 12(b), and their main parameters are reported in Table I. The equivalent grid impedance has been either realized through additional hardware elements between the Regatron TC.ACS and the AFE unit, or has been emulated by using a Plexim RT-Box controlling the Regaton TC. ACS in closed loop. The setup is shown in Fig. 12(d).

Finally, the adopted impedance estimation unit is shown in Fig. 12(c). It is based on LEM IT 60-S Ultrastab current transducers and LEM CV 3-1000V 1:100 voltage modules, while the acquisition device is a 32×14 bits channels Elsys Tranet 408S, with an effective sampling frequency of 1 MHz.

TABLE I
Ratings and Parameters of the Active Front End

Parameter	Value
S	45 kVA
V_{DC}	600 V to 800 V
V_{AC}	400 V (phase-to-phase RMS)
f_{sw}	8 kHz
L_{c}	600 µH
C	100 µF
L_{g}	300 µH

The impedance has been estimated in the *dq* reference frame following the methods developed by [6], [8], [9], [12], [19]. Two separate perturbations have been injected, first on the *d* and then on the *q*-axis, while recording the corresponding grid voltages and currents. The grid angle has then estimated using a conventional phase-locked loop (PLL) algorithm [12], [23], and the recorded grid voltages and currents are transformed in the *dq* reference frame. The frequency components of the perturbations have been extracted using a fast-fourier transform (FFT) algorithm and, finally, the grid impedances matrix has been estimated as described in [24]:

$$Z_{g,dq}(f) = \begin{bmatrix} Z_{g,dd} & Z_{g,qd} \\ Z_{g,dq} & Z_{g,qq} \end{bmatrix} = V_{g,dq}(f) \cdot I_{g,dq}^{-1}(f) \tag{13}$$

where the voltages and currents of the two perturbation injections (here denoted by the superscripts (1) and (2)) have been grouped in matrix form as:

$$V_{g,dq}(f) = \begin{bmatrix} v_{g,d}^{(1)} & v_{g,d}^{(2)} \\ v_{g,q}^{(1)} & v_{g,q}^{(2)} \end{bmatrix}, \; I_{g,dq}(f) = \begin{bmatrix} i_{g,d}^{(1)} & i_{g,d}^{(2)} \\ i_{g,q}^{(1)} & i_{g,q}^{(2)} \end{bmatrix} \tag{14}$$

B. Test at Fixed Frequency

For a first test, the AFE has been connected to a 400 V AC grid, and a purely resistive impedance been emulated as $Z_g = R_g = 2\ \Omega$. The DC-bus voltage has been set to a value of 600 V, which is relatively low considering the AC grid voltage value. The converter has been operated to absorb an active power of 500 W and a reactive power of 5 kVAr. In these operating

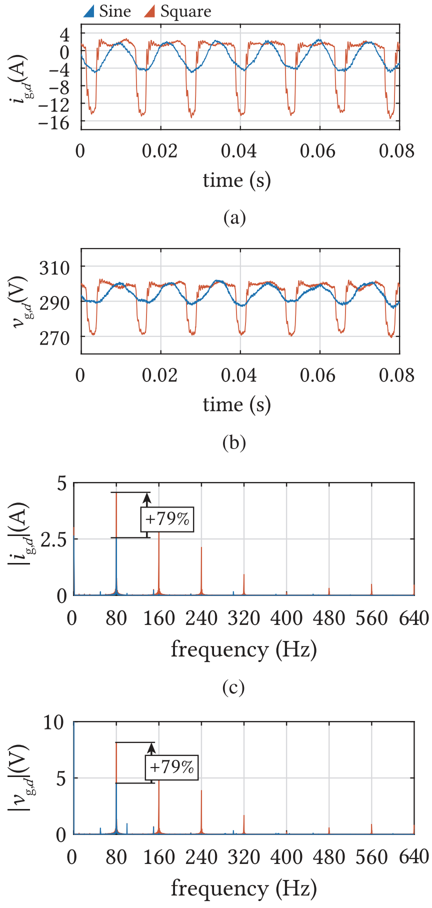

(a)

(b)

(c)

(d)

Fig. 13. Experimental results showing the voltage and current measurements at the PCC obtained by injecting a *d*-axis perturbation at fixed frequency (f_P = 80 Hz). (a),(b) Time domain. (c),(d) Frequency domain, K^+ =10 V, T_{FFT} = 4 s, $T_{\mathrm{injection}}$ = 3.2 s, $T_{\mathrm{relaxation}}$ =0.8 s.

conditions, the a fundamental AC voltage of the converter is equal to 293 V (i.e., modulation index of 0.98), and the available voltage reserve is equal to 53 V.

To estimate the grid impedance, a small signal perturbation has been injected in the *d*-axis of the converter voltages, considering first a single-tone sinusoidal signal and then the proposed asymmetric rectangular signal. In both cases, the fundamental frequency of the perturbation has been set to f_p = 80 Hz, and the maximum magnitude of the perturbation has been set to K^+ = 10 V. This value is used as an exemplary value to demonstrate the method but it could be increased for higher frequencies, where the filter damping effect is stronger and hence the perturbation magnitude needs to be larger. A ratio of (K^-/K^+) = 4 has been considered for the asymmetric perturbation signal.

The results of this test are shown in Fig. 13. They show the measured grid voltage and current.

The results are in line with the theoretical analysis, and show that the asymmetrical perturbation signal, without violating the maximum voltage that can be generated by the converter, can achieve a magnitude increase of around 79% compared to a single-tone perturbation.

The higher magnitude in the voltage and current measurement allows having a more reliable impedance estimation. Considering a random uncertainty in the voltage measurement of ±5 mV and a random uncertainty in the current measurement of ±5 mA (obtained from measurements of the noise level on the analyzed setup), the resistance estimated with the sine injection is $\hat{R}_g = 1.784\ \Omega \pm 5.5\ \mathrm{m}\Omega$ (i.e., with a 0.3% uncertainty in the result), while the resistance estimated with the proposed asymmetric injection is $\hat{R}_g = 1.778\ \Omega \pm 3.0\ \mathrm{m}\Omega$ (i.e., with a 0.17% uncertainty in the result). The difference between the reference and the emulated impedances is caused by the low precision of the grid emulator internal current measurements employed to generate the emulated impedance voltage drop in the grid voltages.

As also previously mentioned in Section III, the higher order harmonics introduced by the asymmetric perturbation injection signal can also be used to estimate the system impedance at the multiple integers of the base frequency f_p = 80 Hz. By referring to the same results shown in Fig. 13 (i.e., without any need for additional experimental recordings), the estimated resistances at 160, 240 and 320 Hz are of $\hat{R}_g = 1.800\ \Omega \pm 4\ \mathrm{m}\Omega$, $\hat{R}_g = 1.829\ \Omega \pm 7\ \mathrm{m}\Omega$ and $\hat{R}_g = 1.813\ \Omega \pm 15\ \mathrm{m}\Omega$, respectively. While it is true that the uncertainty is larger at higher frequencies, this estimation was achieved without any additional measurements. This would have been impossible with a sine wave excitation, highlighting the advantage of the asymmetric perturbation injection as an optimal multi-tone injection for impedance identification across multiple harmonics.

C. Test With a Narrow-Band Perturbation

This test has been executed in the same operating conditions of the previous case. In this case however, the grid impedance has been emulated as a resistance of 1 Ω. Contrarily to the former test, in this case a narrow-bandwidth perturbation has been injected in the *d*-axis of the converter voltages, and a linear frequency sweep has been implemented as in (9) covering the range [70 Hz, 90 Hz] with a rise-time of 1.9 s. The results are reported in Fig. 14, showing the timedomain waveforms and harmonic spectra of the grid voltages and currents. In agreement with the previous analysis, the spectrum obtained with asymmetric signal shows a much higher magnitude compared to the one obtained with the symmetric square-wave injection, with around 85 % higher harmonics in the [70 Hz, 90 Hz] range. On average in this range, the impedance can be estimated with the sine injection is $\hat{R}_g = 0.930\ \Omega \pm 22\ \mathrm{m}\Omega$ (i.e., with a 1.3% uncertainty in the result), while the resistance estimated with the proposed asymmetric injection is $\hat{R}_g = 0.926\ \Omega \pm 12\ \mathrm{m}\Omega$ (i.e., with a 2.3% uncertainty in the result).

Additionally, coherently with the results of Section III-B, significantly stronger higher-order harmonic bands are also present, which can be used to estimate the grid impedance also above the [70 Hz; 90 Hz] band. Considering the same recording shown in Fig. 14 the average resistance estimated in the first three higher order harmonic bands is $\hat{R}_g = 0.957\ \Omega \pm 22\ \mathrm{m}\Omega$, $\hat{R}_g = 0.971\ \Omega \pm 42\ \mathrm{m}\Omega$ and $\hat{R}_g = 0.987\ \Omega \pm 103\ \mathrm{m}\Omega$,

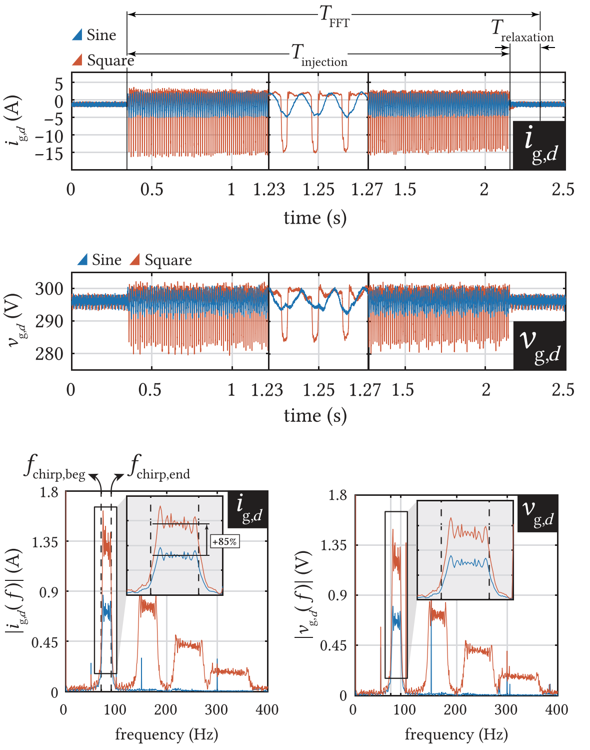

Fig. 14. Time domain waveforms and frequency domain spectra of the grid d-axis current and voltage measured at the PCC in case of a narrow-bandwidth chirp perturbation injection. $[f_{\text{chirp,beg}}, f_{\text{chirp,end}}] = [70\text{ Hz}, 90\text{ Hz}]$ ($K^+ = 10$ V, $T_{\text{FFT}} = 2$ s, $T_{\text{injection}} = 1.9$ s, $T_{\text{relaxation}} = 0.1$ s).

respectively. Once again, these extra results, despite being less precise than the estimation in the base perturbation frequency band, have been obtained without requiring any additional measurement on the system, which would have not been possible with a sine chirp.

D. Wide-Bandwidth Perturbation

A wide-bandwidth perturbation injection has also been performed to evaluate the performances of the proposed approach with the same operating conditions as the narrow-band perturbation (same grid voltage and impedance, same converter operation point, same grid impedance of 1 Ω emulated by the grid emulator). The frequency sweep has been applied between 0 Hz and 1 kHz, which is 1/8th of the switching frequency f_{SW}. The perturbation time interval has been chosen to be 3.2 s, larger than the narrow-bandwidth signal to have higher frequency magnitudes and the peak ratio K^-/K^+ has been varied between 1 and 4. The recorded waveforms of the grid currents and voltages, together with their corresponding harmonic spectra, are plotted in Fig. 15. As it can be seen, in this case as well the proposed asymmetric signal achieves a much higher magnitude compared to a symmetric square-wave perturbation with a peak magnitude around 140% larger.

Fig. 16 shows the results of the impedance estimation performed with the measured data. The impedance $Z_{\text{g}}^{\text{est}}$ est is plotted along with its filtered value Z_{m} and its standard deviation (or uncertainty) Z_{σ}. The computation of Z^{est}, Z_{m} and Z_{σ} is described further in the appendices.

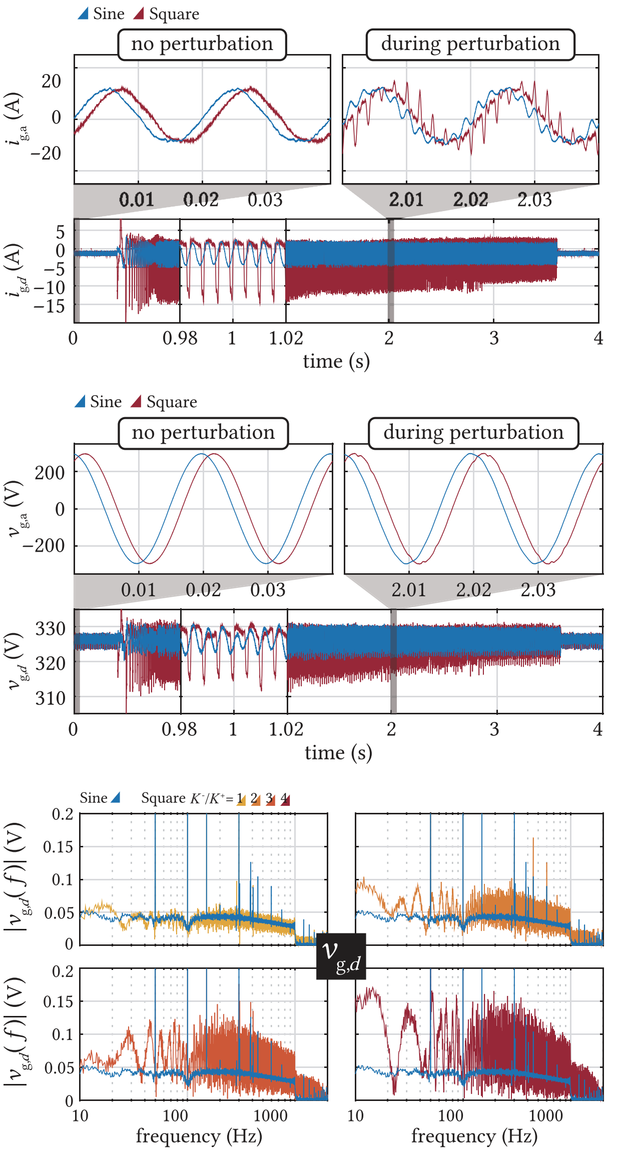

Fig. 15. Time domain waveforms and frequency domain spectra of the grid d-axis current and voltage measured at the PCC in case of a wide-bandwidth chirp perturbation injection. $[f_{\text{chirp,beg}}, f_{\text{chirp,end}}] = [0\text{ Hz}, 1000\text{ Hz}]$ ($K^+ = 10$ V, $T_{\text{FFT}} = 4$ s, $T_{\text{injection}} = 3.2$ s, $T_{\text{relaxation}} = 0.8$ s).

The figures show a significant improvement in the impedance estimation when the impedance is estimated by the asymmetric square chirp signal with respect to the estimation obtained with the sine chirp signal. In the case of the sine chirp signal, the impedance amplitude of $Z_{g,dd}$ is estimated with an uncertainty of 35 mΩ on average (around 4% uncertainty). In the case of the asymmetric square chirp signal, the impedance amplitude is estimated with an uncertainty of 23 mΩ on average. This gives an improvement of the magnitude estimation of 37%. On the other hand, since the impedance $Z_{g,qq}$ is mostly impacted by the injection in the q-axis, the uncertainty is relatively constant for both perturbation scenarios (when the perturbation in the d is a sine chirp, the uncertainty

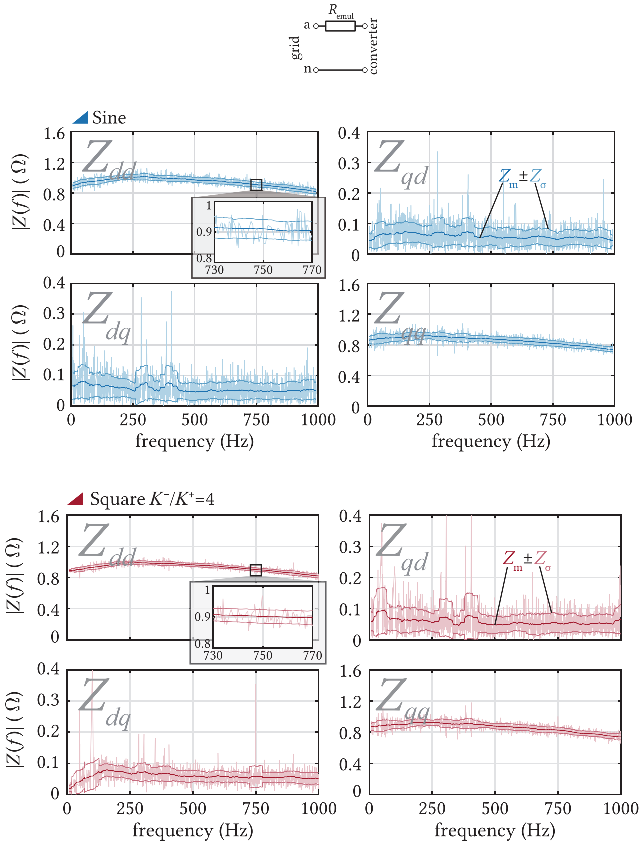

Fig. 16. Impedance estimation for an emulated grid impedance $Z_{g,emul} = R_g$ of 1 Ω using a wide-band perturbation signal. $[f_{chirp,beg}, f_{chirp,end}] = [0\ \text{Hz}, 1000\ \text{Hz}]$, *d*-axis injection: sine chirp or square chirp with $K_d^+ = 10$ V, *q*-axis injection: sine chirp with $K_q^+ = 10$ V, $T_{FFT} = 4$ s ($T_{injection} = 3.2$ s, $T_{relaxation} = 0.8$ s).

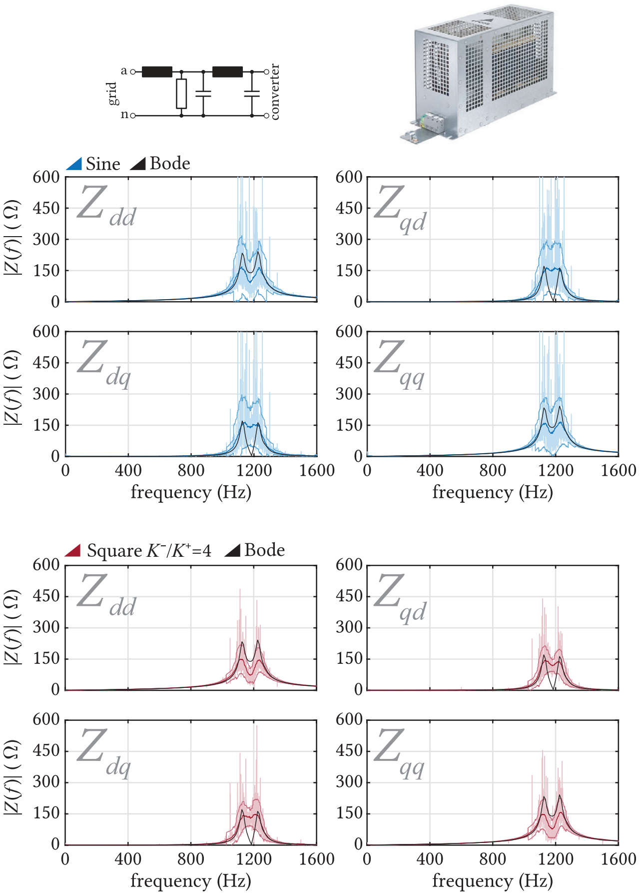

Fig. 17. Impedance estimation for a commercial LC filter (EPCOS B84143V0033R127) using a wide-band perturbation signal. $[f_{chirp,beg}, f_{chirp,end}] = [0\ \text{Hz}, 1600\ \text{Hz}]$, *d*-axis injection: sine chirp or square chirp with $K_d^+ = 5$ V, *q*-axis injection: sine chirp with $K_q^+ = 10$ V ($T_{FFT} = 4$ s, $T_{injection} = 3.2$ s, $T_{relaxation} = 0.8$ s).

is of only 43 mΩ and when it is a square chirp, the uncertainty 42 mΩ on average). Finally, as for the cross-coupling, the improvement on the estimation is only significant in the *dq* term (–31% when the square chirp is employed compared to when the sine chirp is employed). The *qd* impedance term, mainly impacted by the injection in the *q*-axis is almost not affected by the change in perturbation in the *d*-axis (–0.1%).

Additional impedance estimation have been performed to corroborate the results detailed previously. With the same operating conditions (600 V on the DC-bus voltage, 500 W and 5 kVAr active and reactive power absorbed by the converter), a commercial LC filter from EPCOS has been inserted in the grid (grid emulator is then emulating an ideal grid voltage source). Results are shown in Fig. 17 and compared to offline measurements acquired by the Bode 100 impedance analyzer. The estimation uncertainty for the Z_{dd} term has been reduced by 24% and the for the Z_{dq} term, the estimation has also been improved by a similar factor (31%). The impedance terms Z_{qd} and Z_{qq} are witnessing minor changes in the estimation uncertainty (from +3% to –10%).

Then, to show that the proposed perturbation injection does not affect the AFE operating point, the DC-bus voltage has been increased to 705 V and an inductive impedance has been estimated in two conditions: one when the AFE converter is transferring 3 kW to the AC grid and one when the AFE is transferring 20 kW instead. Results can be found in Figs. 18 and 19. As seen also in this case, the estimation is improved when the square asymmetric perturbation signal is employed. The uncertainty on the *dd* impedance has improved by 24% and 21% respectively.

This illustrates the merits of the asymmetric signal, offering impedance estimation improvements when the voltage reserve is limited: caused either by a limited DC-bus voltage, as in Figs. 16 and 17 or by a high power processing operation, as in Figs. 18 and 19. As a result, to achieve high signal-to-noise ratio, the only method is to generate a perturbation of larger negative magnitude.

Table II provides a quick summary of the obtained experimental results in case of wide-bandwidth perturbation, where are plotted the average impedance uncertainty in percentage. As it can be seen, the *dd* and *dq* impedances are the ones where the estimation has the most improved with an uncertainty by 26% and up to 55%. The *qd* and *qq* terms are the impedances who have the least improvement, since they are mostly affected by the injection in the *q*-axis (same injection

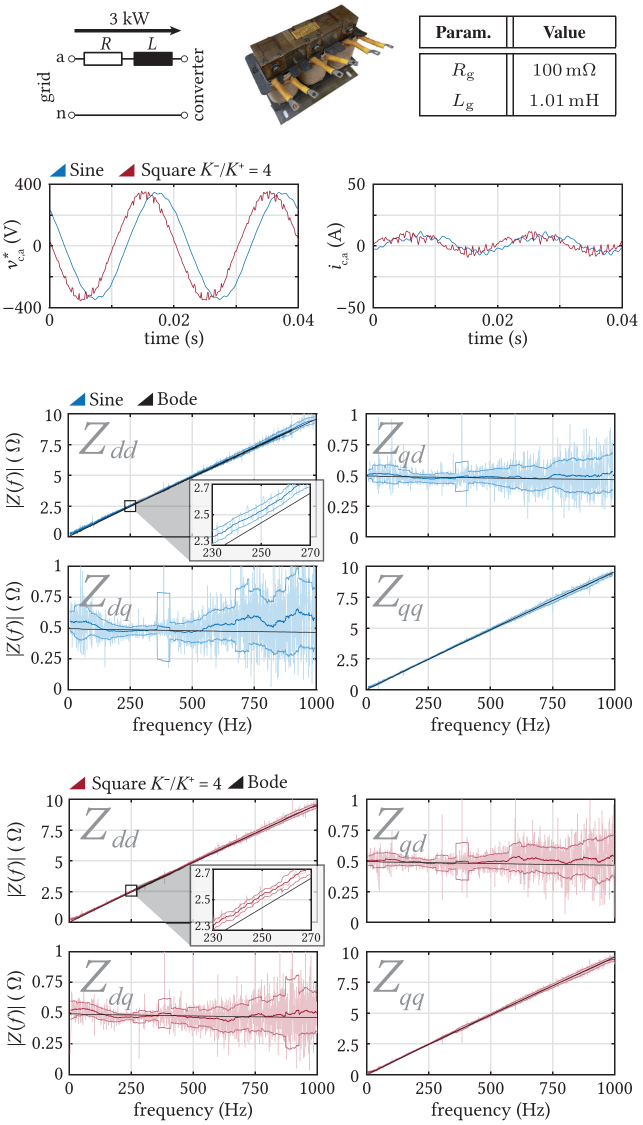

Fig. 18. Top)voltage reference and measured converter current on phase a. 3 kW are processed from the AC grid to the converter. Bottom) Impedance estimation for an inductive grid impedance using a wide-band perturbation signal. $[f_{\text{chirp,beg}}, f_{\text{chirp,end}}]$ = [0 Hz, 1000 Hz], *d*-axis injection: sine chirp or square chirp with $K_d^+ = 5$ V, *q*-axis injection: sine chirp with $K_q^+ = 10$ V ($T_{\text{FFT}} = 4$ s, $T_{\text{injection}} = 3.2$ s, $T_{\text{relaxation}} = 0.8$ s).

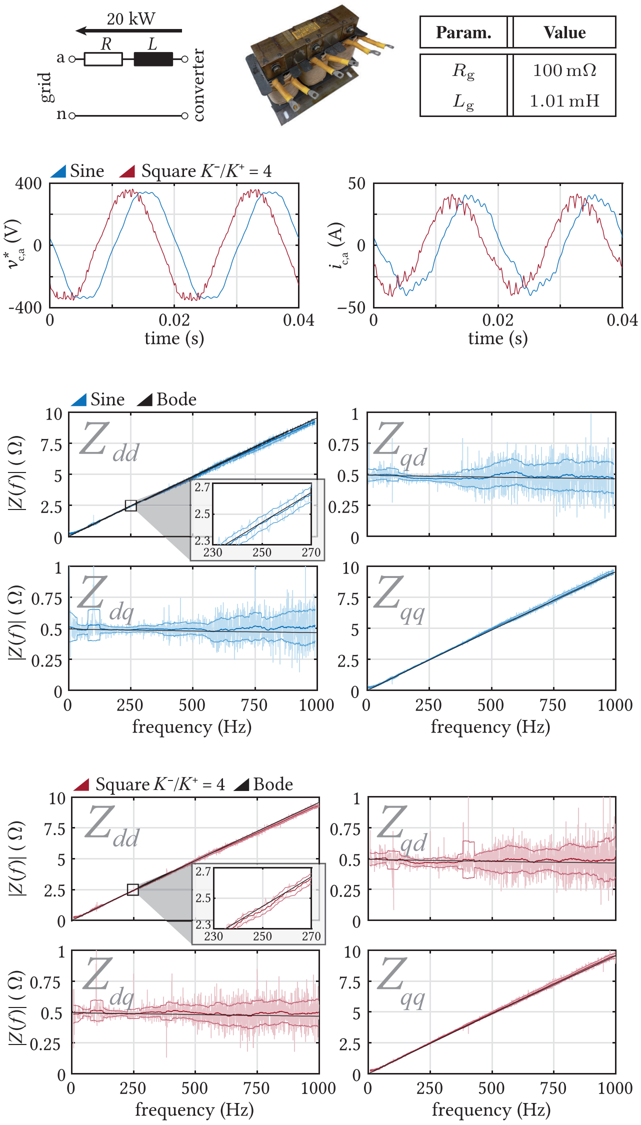

Fig. 19. Top)voltage reference and measured converter current on phase a. 20 kW are processed from the converter to the AC grid. Bottom) Impedance estimation for an inductive grid impedance using a wide-band perturbation signal. $[f_{\text{chirp,beg}}, f_{\text{chirp,end}}]$ = [0 Hz, 1000 Hz], *d*-axis injection: sine chirp or square chirp with $K_d^+ = 5$ V, *q*-axis injection: sine chirp with $K_q^+ = 10$ V ($T_{\text{FFT}} = 4$ s, $T_{\text{injection}} = 3.2$ s, $T_{\text{relaxation}} = 0.8$ s).

TABLE II

AVERAGE IMPEDANCE IDENTIFICATION UNCERTAINTY IN THE ANALYZED EXPERIMENTAL RESULTS

Impedance →	Z_{dd}			Z_{dq}			Z_{qd}			Z_{qq}		
Operating Condition ↓	Sine		Square	Sine		Square	Sine		Square	Sine		Square
Emulated 1 ohm Resistance	0.0369	$\xrightarrow[-46\%]{}$	0.0252	0.5187	$\xrightarrow[-38\%]{}$	0.3771	0.5917	$\xrightarrow[+3\%]{}$	0.6106	0.0501	$\xrightarrow[-3\%]{}$	0.0488
LC filter	0.2274	$\xrightarrow[-50\%]{}$	0.1515	0.4713	$\xrightarrow[-44\%]{}$	0.3275	0.3413	$\xrightarrow[-13\%]{}$	0.3028	0.2304	$\xrightarrow[-16\%]{}$	0.1992
RL filter (rectifier mode)	0.0416	$\xrightarrow[-55\%]{}$	0.0268	0.2697	$\xrightarrow[-38\%]{}$	0.1951	0.1674	$\xrightarrow[+2\%]{}$	0.1714	0.0338	$\xrightarrow[-2\%]{}$	0.0330
RL filter (inverter mode)	0.0337	$\xrightarrow[-26\%]{}$	0.0268	0.1441	$\xrightarrow[-3\%]{}$	0.1403	0.1563	$\xrightarrow[+9\%]{}$	0.1719	0.0290	$\xrightarrow[-0\%]{}$	0.0289

Note: Values displayed are computed as mean(Z_σ/Z_m) with $Z = \{Z_{dd}, Z_{dq}, Z_{qd}, Z_{qq}\}$

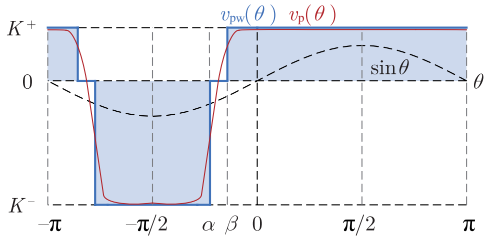

Fig. 20. Examples of an asymmetric perturbation function $v_p(\theta)$ and the corresponding piece-wise linear function $v_{pw}(\theta)$.

amplitude in both test conditions).

V. CONCLUSION

The impedance identification in AC networks, whether for the grid itself or for a grid-connected device, requires the injection of controlled small-signal perturbations and the analysis of the corresponding small-signal responses. Using existing grid-connected converters as perturbation injection sources is advantageous for enabling impedance estimation without the need for installing additional dedicated hardware.

Nevertheless, most existing grid-connected converters are designed to operate with a small voltage reserve, which severely limits the magnitude of the perturbation that can be injected into the system. This effect is even worsened by the attenuation introduced by filtering elements between the converter and the grid. In practice, if the magnitude of injected harmonics is too low, the effect of measuring uncertainty or sensor noise could lead to an unreliable impedance estimation.

However, commonly adopted perturbation signals do not optimally utilize the limited available voltage reserve, which could be instead better exploited by using asymmetric signals. This paper investigated the selection of an optimal perturbation injection signal to maximize the utilization of a limited available voltage reserve of a grid-connected converter.

It has been shown that the optimal perturbation signal is an asymmetric rectangular wave with different positive and negative values, and that this signal can achieve up to a 100% increase in the magnitude of the fundamental perturbation harmonic compared to a single-tone signal, and up to a 55% increase compared to a symmetrical square-wave signal.

The proposed approach has also been extended to generate a chirp perturbation, by implementing a frequency sweep over a desired range. The effects of different peak ratios, frequency bands and sweep rising times have been discussed, and it has been shown that in all these operating conditions the proposed asymmetric rectangular signal can achieve higher perturbation magnitudes compared to a conventional sine chirp.

Finally, the proposed technique has been tested experimentally, validating the analytical results, and can reduce the grid impedance estimation uncertainty by up to 30%.

ACKNOWLEDGMENTS

The results presented in this paper are a part of the HYPERRIDE project that has received funding under the European Union's Horizon 2020 research and innovation programme (Grant agreement No. 957788).

APPENDIX A

PROOF FOR THE OPTIMAL ASYMMETRIC SIGNAL SHAPE

In what follows, it is analytically proven that the asymmetric square wave signal $v_{p,opt}(t)$, whose expression is provided in (6), is the optimal solution of the optimization problem (3).

For the proof, it is assumed that the limits $K^+ > 0$ and $K^- < 0$ are constant, and that $|K^-| > |K^+|$ (as it is the case for perturbations superimposed on top of the fundamental voltage waveforms in a grid-connected converter). Furthermore, the dependence on a specific perturbation frequency f_p is omitted by considering the substitution $t \rightarrow \theta$, with $\theta = 2\pi f_p t$, corresponding to a normalization in time.

In order for a periodic function $v_p(\theta)$ to maximize the magnitude of its fundamental component, it must maximize the correlation with the sinusoidal function $\sin\theta$ in the interval $[-\pi, +\pi]$. However, since the desired function $v_p(\theta)$ must guarantee zero average value, the area spanned in the positive sign must be equal to the area spanned under the negative sign.

From any function $v_p(\theta)$ limited in the range $[K^-, K^+]$, it is always possible to find an equivalent piece-wise linear function $v_{pw}(\theta)$ that only assumes the values K^-, 0 and K^+, and that has the same average value and the same magnitude of the fundamental component as $v_p(\theta)$. A graphical example is given in Fig. 20. For symmetry reason, the behavior of this function can be analyzed in the interval $[-\pi/2, +\pi/2]$. Then, the average value of $v_{pw}(\theta)$ is computed as:

$$\begin{aligned} M &= \frac{1}{2\pi}\int_{-\pi}^{+\pi} v_{pw}(\theta)\,d\theta = \frac{2}{2\pi}\int_{-\pi/2}^{+\pi/2} v_{pw}(\theta)\,d\theta \\ &= \frac{1}{\pi}\left(\int_{-\pi/2}^{\alpha} K^- d\theta + \int_{\alpha}^{\beta} 0 d\theta + \int_{\beta}^{\pi/2} K^+ d\theta\right) \\ &= \frac{1}{\pi}\left[K^-\left(\alpha + \frac{\pi}{2}\right) + K^+\left(\frac{\pi}{2} - \beta\right)\right] \end{aligned} \tag{15}$$

Similarly, the magnitude of the fundamental component of $v_{pw}(\theta)$ is computed as:

$$\begin{aligned} F &= \frac{2}{2\pi}\int_{-\pi}^{+\pi} v_{pw}(\theta)\sin\theta\,d\theta = \frac{4}{2\pi}\int_{-\pi/2}^{+\pi/2} v_{pw}(\theta)\sin\theta\,d\theta \\ &= \frac{2}{\pi}\left(\int_{-\pi}^{\alpha} K^- \sin\theta\,d\theta + \int_{\alpha}^{\beta} 0\sin\theta\,d\theta + \cdots + \int_{\beta}^{\pi/2} K^+ \sin\theta\,d\theta\right) \\ &= \frac{2}{\pi}\left(-K^- \cos\alpha + K^+ \cos\beta\right) \end{aligned} \tag{16}$$

Since the average value of the original function $v_p(\theta)$ is equal to zero, from (15) it is possible to set the constraint $M = 0$, from which it is possible to obtain the expression of the angle β as a function of the angle α, as:

$$\beta = \left(\frac{K^-}{K^+}\right)\alpha + \left(\frac{K^- + K^+}{K^+}\right)\frac{\pi}{2} \tag{17}$$

Then, by replacing (17) in (16), the magnitude of the fundamental component of $v_{\mathrm{pw}}(\theta)$ can be expressed as:

$$F = \frac{2}{\pi}\left\{K^{-}\cos\alpha - K^{+}\cos\left[\left(\frac{K^{-}}{K^{+}}\right)\alpha + \left(\frac{K^{-}+K^{+}}{K^{+}}\right)\frac{\pi}{2}\right]\right\} \tag{18}$$

The maximum possible value of the fundamental component F with respect to α and setting it to be zero. By taking apart the coefficient (2/π), this results in:

$$\begin{aligned}\frac{\pi}{2}\cdot\frac{\mathrm{d}F}{\mathrm{d}\alpha} &= K^{-}\sin\alpha + \left(\frac{K^{-}}{K^{+}}\right)\cdot\cdots\cdot\sin\left[\left(\frac{K^{-}}{K^{+}}\right)\alpha + \left(\frac{K^{-}+K^{+}}{K^{+}}\right)\frac{\pi}{2}\right] \\ &= K^{-}\cdot[\sin\alpha - \sin\beta] = 0 \end{aligned} \tag{19}$$

Therefore, the stationary points of F as a function of α can be obtained for $\sin\alpha = \sin\beta$, and the maximum is obtained for $\alpha = \beta$. In this case, the function $v_{\mathrm{pw,opt}}(\theta)$ immediately transitions between K^{-} and K^{+}, without having intervals for which it is zero.

Since, as previously stated, all functions $v_{\mathrm{p}}(\theta)$ can be associated to a corresponding piece-wise linear function $v_{\mathrm{pw}}(\theta)$, it can be concluded that $v_{\mathrm{pw,opt}}(\theta)$ is the function that achieves the highest magnitude of the fundamental component among all the considered ones, and it is therefore the optimal solution of the problem (3).

APPENDIX B

Computation of Z^{est}, Z_{m} and Z_{σ}

In this appendix, more details are given related to the impedance estimation procedure of Section IV-D. In this section, the impedance $Z^{\mathrm{est}}_{\mathrm{g},dd}$ is analyzed further in details and it is said that it can be estimated by an impedance Z_{m} with an error of Z_{σ}.

$Z^{\mathrm{est}}(f)$ is computed following the method presented in (13) using the voltages and currents $v_{\mathrm{g},dq}(f_i)$ and $i_{\mathrm{g},dq}(f_i)$ for the all the frequency points f_i where $|v_{\mathrm{g},d}(f_i)|$ is above the moving average $|v_{\mathrm{g},d,\mathrm{m}}(f_i)|$.

$$\left|v_{\mathrm{g},d,\mathrm{m}}(f_i)\right| = \frac{1}{101}\sum_{k=i-50}^{i+50}\left|v_{\mathrm{g},d}(f_k)\right| \tag{20}$$

In other words, are taken only 50 % of the frequency points with the highest magnitude, relatively to the average magnitude. Finally, the impedance outliers are removed by discarding all the points that are significantly higher or lower than the average value (for which $|Z^{\mathrm{est}}(f)|$ is above two times the average impedance value $|Z^{\mathrm{est}}_{\mathrm{m}}(f)|$ for instance).

Z_{m} is obtained by a moving average on a 100 points window:

$$\left|Z_{\mathrm{m}}(f_i)\right| = \frac{1}{101}\sum_{k=i-50}^{i+50}\left|Z^{*}(f_k)\right| \tag{21}$$

The standard deviation is computed by comparing the curves of Z^{est} and Z_{m}. Hence, assuming the impedance is following a Gaussian distribution, the impedance is estimated with the 68% confidence on the interval $[Z_{\mathrm{m}} - Z_{\sigma}, Z_{\mathrm{m}} + Z_{\sigma}]$, with the standard deviation computed based on the difference between Z_{m} and Z^{est}:

$$\left|Z_{\sigma}(f_i)\right| = \sqrt{\frac{1}{101}\sum_{k=i-50}^{i+50}\left[\left|Z^{*}(f_k) - Z_{\mathrm{m}}(f_k)\right|\right]^{2}} \tag{22}$$

With N being the number of frequency points of Z^{est}. The standard deviation is hence also termed in the paper as uncertainty as the impedance can be estimated as $Z_{\mathrm{m}} \pm Z_{\sigma}$ with a 68% confidence in the entire frequency range of perturbation.

REFERENCES

[1] E. Mollerstedt and B. Bernhardsson, "Out of control because of harmonics-An analysis of the harmonic response of an inverter locomotive," in *IEEE Control Systems Magazine*, vol. 20, no. 4, pp. 70–81, Aug. 2000.

[2] H. Saad, Y. Fillion, S. Deschanvres, Y. Vernay, and S. Dennetière, "On resonances and harmonics in HVDC-MMC station connected to AC grid," in *IEEE Transactions on Power Delivery*, vol. 32, no. 3, pp. 1565–1573, Jun. 2017.

[3] L. Asiminoaei, R. Teodorescu, F. Blaabjerg, and U. Borup, "A digital controlled PV-inverter with grid impedance estimation for ENS detection," in *IEEE Transactions on Power Electronics*, vol. 20, no. 6, pp. 1480–1490, Nov. 2005.

[4] A. Knop and F. W. Fuchs, "High frequency grid impedance analysis by current injection," in *Proceedings of 2009 35th Annual Conference of IEEE Industrial Electronics*, pp. 536–541, Nov. 2009.

[5] T. Roinila, M. Vilkko, and J. Sun, "Online grid impedance measurement using discrete-interval binary sequence injection," in *IEEE Journal of Emerging and Selected Topics in Power Electronics*, vol. 24, no. 4, pp. 985–993, Dec. 2014.

[6] A. Riccobono, M. Mirz, and A. Monti, "Noninvasive online parametric identification of three-phase AC power impedances to assess the stability of grid-tied power electronic inverters in LV networks," in *IEEE Journal of Emerging and Selected Topics in Power Electronics*, vol. 6, no. 2, pp. 629–647, Jun. 2018.

[7] M. Ciobotaru, R. Teodorescu, and F. Blaabjerg, "On-line grid impedance estimation based on harmonic injection for grid-connected PV inverter," in *Proceedings of 2007 IEEE International Symposium on Industrial Electronics*, pp. 2437–2442, Jun. 2007.

[8] M. Céspedes and J. Sun, "Online grid impedance identification for adaptive control of grid-connected inverters," in *Proceedings of 2012 IEEE Energy Conversion Congress and Exposition (ECCE),* Raleigh, NC, USA, pp. 914–921, Sept. 2012.

[9] A. Ghanem, M. Rashed, M. Sumner, M. A. Elsayes, and I. I. Mansy, "Grid impedance estimation for islanding detection and adaptive control of converters," in *IET Power Electronics*, vol. 10, no. 11, pp. 1279–1288, 2017.

[10] Z. Ling, J. Xu, Y. Wu, Y. Hu, and S. Xie, "Adaptive tuning of phase-locked loop parameters for grid-connected inverters in weak grid cases," in *Proceedings of 2021 IEEE 16th Conference on Industrial Electronics and Applications (ICIEA)*, pp. 821–826, Aug. 2021.

[11] M. Li, H. Nian, Y. Wang, D. Sun, H. Li, and H. Li, "Over-modulation risk evaluation method in impedance measurement for peak-value constrain," in *Proceedings of IECON 2023- 49th Annual Conference of the IEEE Industrial Electronics Society*, pp. 1–6, Oct. 2023.

[12] G. Francis, R. Burgos, D. Boroyevich, F. Wang, and K. Karimi, "An algorithm and implementation system for measuring impedance in the DQ

domain," in *Proceedings of 2011 IEEE Energy Conversion Congress and Exposition*, pp. 3221–3228, Sept. 2011.

[13] H. Gong, X. Wang, and D. Yang, "DQ-frame impedance measurement of three-phase converters using time-domain MIMO parametric identification," in *IEEE Transactions on Power Electronics*, vol. 36, no. 2, pp. 2131–2142, Feb. 2021.

[14] Z. Xie, W. Wu, Y. Chen, S. Cao, Y. Fu, and S. Liang, "Switching control and its experimental verification of megawatt high-voltage impedance measurement equipment," in *Proceedings of 2021 IEEE Sustainable Power and Energy Conference (iSPEC)*, pp. 3188–3193, Dec. 2021.

[15] L. Fan, Z. Miao, P. Koralewicz, S. Shah, and V. Gevorgian, "Identifying DQ-domain admittance models of a 2.3-MVA commercial grid-following inverter via frequency-domain and time-domain data," in *IEEE Transactions on Energy Conversion*, vol. 36, no. 3, pp. 2463–2472, Sept. 2021.

[16] T. Roinila, T. Messo, and E. Santi, "MIMO-identification techniques for rapid impedance-based stability assessment of three-phase systems in DQ domain," in *IEEE Transactions on Power Electronics*, vol. 33, no. 5, pp. 4015–4022, May 2018.

[17] D. Martin, E. Santi, and A. Barkley, "Wide bandwidth system identification of AC system impedances by applying pertubations to an existing converter," in *Proceedings of 2011 IEEE Energy Conversion Congress and Exposition*, pp. 2549–2556, Sept. 2011.

[18] M. Tsukamoto, S. Ogawa, Y. Natsuda, Y. Minowa, and S. Nishimura, "Advanced technology to identify harmonics characteristics and results of measuring," in *Proceedings of Ninth International Conference on Harmonics and Quality of Power. Proceedings (Cat. No.00EX441)*, vol. 1, pp. 341–346, Oct. 2000.

[19] Z. Shen, M. Jaksic, P. Mattavelli, D. Boroyevich, J. Verhulst, and M. Belkhayat, "Three-phase AC system impedance measurement unit (IMU) using chirp signal injection," in *Proceedings of 2013 Twenty-Eighth Annual IEEE Applied Power Electronics Conference and Exposition (APEC)*, pp. 2666–2673, Mar. 2013.

[20] W. Uddin, T. Husain, R. Mitra, E. Ofori, Y. Sozer, and I. Husain, "A chirp PWM scheme for brushless DC motor drives," in *Proceedings of 2012 IEEE Energy Conversion Congress and Exposition (ECCE)*, pp. 3317–3323, Sept. 2012.

[21] H. Hu, P. Pan, Y. Song, and Z. He, "A novel controlled frequency band impedance measurement approach for single-phase railway traction power system," in *IEEE Transactions on Industrial Electronics*, vol. 67, no. 1, pp. 244–253, Jan. 2020.

[22] P. Pan, H. Hu, D. Xiao, Y. Song, and Z. He, "An improved controlled of requency-band impedance measurement scheme for railway traction power system," in *IEEE Transactions on Industrial Electronics*, vol. 68, no. 3, pp. 2184–2195, Mar. 2021.

[23] Z. Shen, M. Jaksic, B. Zhou, P. Mattavelli, D. Boroyevich, J. Verhulst, and M. Belkhayat, "Analysis of phase locked loop (PLL) influence on DQ impedance measurement in three-phase AC systems," in *Proceedings of 2013 Twenty-Eighth Annual IEEE Applied Power Electronics Conference and Exposition (APEC)*, pp. 939–945, Mar. 2013.

[24] M. Jaksic, Z. Shen, I. Cvetkovic, D. Boroyevich, R. Burgos, and P. Mattavelli, "Wide-bandwidth Identification of small-signal DQ impedances of AC power systems via single-phase series voltage injection," in *Proceedings of 2015 17th European Conference on Power Electronics and Applications (EPE'15 ECCE-Europe)*, pp. 1–10, Sept. 2015.

Jules Mace received the B.S. and M.Sc. degrees in electrical engineering from the National Institute of Applied Sciences (INSA) of Toulouse, France, in 2020, and the M.Sc. degree from the Seoul National University, South Korea, in 2020. He is a Ph.D. student with the Power Electronics Laboratory, École Polytechnique Fédérale de Lausanne, Switzerland since 2020. His research interests include power converter modeling and design, system identification and stability in hybrid AC/DC power distribution networks.

Andrea Cervone received the B.Sc., M.Sc., and Ph.D. degrees in electrical engineering from the University of Naples Federico II, Naples, Italy, in 2014, 2017, and 2021, respectively. He is currently a post-doc at the Power Electronics Laboratory of the École Polytechnique Fédérale de Lausanne (EPFL). His research interests include modeling and control of power electronics converters and electrical drives.

Drazen Dujic received the Dipl.Ing. and M.Sc. degrees in electrical engineering from the University of Novi Sad, Novi Sad, Serbia, in 2002 and 2005, respectively, and the Ph.D. degree in electrical engineering from Liverpool John Moores University, Liverpool, U.K., in 2008. From 2002 to 2006, he was with the Department of Electrical Engineering, University of Novi Sad as a Research Assistant. From 2006 to 2009, he was with Liverpool John Moores University as a Research Associate. From 2009 to 2013, he was with the ABB Corporate Research Centre, Switzerland, as the Principal Scientist working on the power electronics projects spanning the range from low-voltage/power SMPS in below kilowatt range to medium voltage high-power converters in a megawatt range. From 2010 to 2011, he was a Member of a project team responsible for the development of the world's first power electronic traction transformer successfully commissioned on the locomotive. From 2013 to 2014, he was with ABB Medium Voltage Drives, Turgi, Switzerland, as a Research and Development Platform Manager responsible for ABB's largest IGCT-based medium voltage drive ACS6000. He is currently with the École Polytechnique Fédérale de Lausanne, Lausanne, Switzerland, as an Associate Professor and the Director of the Power Electronics Laboratory. He has authored or coauthored more than 200 scientific publications and has filed 18 patents. His current research interests include the areas of design and control of advanced high-power electronics systems for medium voltage applications. Dr. Dujic has received the First Prize Paper Award from the Electric Machines Committee of the IEEE Industrial Electronics Society, in 2007, the Isao Takahashi Power Electronics Award for Outstanding Achievement in Power Electronics in 2014, and the EPE Outstanding Service Award from the European Power Electronics and Drives Association in 2018. He is an Associate Editor of the *IEEE Transactions on Power Electronics*.